



# Alkali-assisted fabrication of holey carbon nitride nanosheet with tunable conjugated system for efficient visible-light-driven water splitting

Ting Song, Piyong Zhang, Tingting Wang, Atif Ali, Heping Zeng\*

Key Laboratory of Functional Molecular Engineering of Guangdong Province, School of Chemistry and Chemical Engineering, South China University of Technology, Guangzhou 510641, PR China

## ARTICLE INFO

### Keywords:

Graphitic carbon nitride  
Water splitting  
Visible light  
In-plane hole  
Conjugated system

## ABSTRACT

Graphitic carbon nitride (CN) nanosheets have aroused a great deal of interest due to their capability to utilize visible light to split water into its constituent molecules of hydrogen and oxygen ( $H_2$  and  $O_2$ ). However, the photocatalytic capacity of conventional bulk  $g-C_3N_4$ , with its large  $\pi$ - $\pi$  conjugated electronic system, is still constrained by the  $\pi$ - $\pi$  stacking interaction and small number of active sites. Hence, an uncomplicated post-processing method to construct a different  $\pi$ - $\pi$  conjugated electronic system of holey CN nanosheets using alkali etching of bulk CN (CN (B)) at 300 °C for 1 h has been developed. Among such compounds, the optimal alkali treatment bulk CN (CN 3(2)) exhibits a suitable conjugated system and copious in-plane holes, and it retains the ability to absorb sunlight during alkali depolymerization. Compared to CN (B), the resultant CN 3(2) has a distensible bandgap of 2.66 eV associated with a much larger specific surface area of  $265.2 \text{ m}^2 \text{ g}^{-1}$ . However, excessive alkali treatment significantly decrease the visible light absorbance and the photocatalytic properties of the CN nanosheet, which demonstrated that a suitable  $\pi$ - $\pi$  conjugated electronic system is very important in allowing the process to proceed. As such, the photocatalytic  $H_2$  and  $O_2$  production rate of CN 3(2) was nearly 24.6 times that of CN (B) with the addition of carbon quantum dots (CQDs) and Pt.

## 1. Introduction

With increasing concern about the prevalent energy crisis and environmental pollution, the feasibility of using hydrogen ( $H_2$ ) as an alternate source of fuel is receiving a considerable attention all over the world [1,2]. As one of the prospective technologies being actively considered, solar-energy-driven  $H_2$  generation plays a considerable role in  $H_2$  production as a renewable and clean energy source that could help to reduce fossil fuel utilization [3–5]. In the last few decades, many kinds of materials have been utilized for photocatalytic  $H_2$  production [6]. Among these, graphitic carbon nitride ( $g-C_3N_4$ ) has emerged as an attractive material for photocatalytic water splitting under visible light irradiation due to its unique properties including suitable energy band structure for redox reaction, high thermal and chemical stability, and cost-effective and metal-free composition [7–10]. However, commonly  $g-C_3N_4$  obtained by the direct thermal polymerization method generally exhibits only moderate photocatalytic activity due to fast electron-hole recombination and low specific surface area, which significantly hinders its applications [11,12]. Recently, many researcher focused on resolving the above drawbacks of  $g-C_3N_4$  took two main approaches. One approach was to ameliorate the band gap and change the electron

structures by doping with heteroatoms [13], modifying with nitrogen vacancies [14], constructing heterojunctions with other semiconductor materials [15], or introducing functional groups [16]. The alternative approach was the preparation of different carbon nitrogen nanostructures with optimized optical and physicochemical performance, by the inclusion of nanosheets [17], nanoparticles [18], nanorods [19], nanotubes [20], nanoribbons [21], nanospheres [22], “seaweed” [23], three-dimensional (3D) belt network, etc [24].

In particular, much attention has been focused on 2D  $g-C_3N_4$  nanosheets, because of their strikingly large specific surface area, improved electron mobility along the in-plane direction, and enhanced electron-phonon interaction [25–27]. Unfortunately, 2D  $g-C_3N_4$ , which is dominated by  $\pi$ - $\pi$  stacking, is more likely to incorporate considerable stacked layered and aggregation structures, which have a negative impact on electron migration and overall water splitting capability [28,29]. Consequently, the key to resolving these issues lies in promoting an increase in the specific surface area, modifying the  $\pi$ - $\pi$  conjugated electronic system, and enlarging the separation of photo-generated electron and hole to improve photocatalytic activity. As is known, it is difficult to synthesize different conjugated systems of graphitic carbon nitride materials by the commonly used thermal

\* Corresponding author.

E-mail address: [hpzeng@scut.edu.cn](mailto:hpzeng@scut.edu.cn) (H. Zeng).

polymerization method (i.e., the direct heating of melamine to 550 °C for 4 h) [30]. Therefore, although there have been many scientific studies that addressed the preparation of 2D CN materials, the synthesis of holey CN nanosheets with suitable conjugated system is still a great challenge. A new method of post-processing can be used to prepare different conjugated systems of CN nanosheets, in which the  $\pi$ - $\pi$  stacking interaction is decreased. The process of alkali etching can change the conjugated systems of g-C<sub>3</sub>N<sub>4</sub>, which is useful for decreasing the  $\pi$ - $\pi$  stacking interaction. Interestingly, the same alkali etching process also forms a lot of in-plane holes, due to the corrosiveness of the alkali to the elemental carbon ( $6\text{KOH} + 2\text{C} \leftrightarrow 2\text{K} + 3\text{H}_2 + 2\text{K}_2\text{CO}_3$ ) [31]. Under these circumstances, holey CN nanosheets with carbon vacancies have many in-plane holes, which are quite commodious and can notably enhance the delivery of charge and mass transfer across the CN planes during the photocatalytic reaction. More extensively, these open pores not only significantly obstruct the aggregation of CN nanosheets by drastically decreasing the number of interaction sites, but also effectively enhance the number of uncovered active locations [32].

In this work, a novel one step KOH-assisted route to prepare different conjugated systems of CN nanosheets with the distinct  $\pi$ - $\pi$  conjugated electronic system is described. Furthermore, CN (B) was successfully stripped into nanosheets with copious in-plane holes and carbon vacancies using this method. Meanwhile, the suitable  $\pi$ - $\pi$  conjugated electronic system of CN 3(2) not only lessens the incidence of aggregation and stacked layered structures but also preserves the ability to absorb sunlight. Moreover, the in-plane holes offer more new cross-plane diffusion channels and active edges, which can significantly accelerate the mass diffusion and transfer of photo-produced charge carriers. The synthesis strategy introduced here thus provides a simple and effective way of synergistically optimizing the chemical composition, optical response, and photocatalytic properties of CN nanosheets.

## 2. Experimental section

### 2.1. Reagents

Triethanolamine, melamine, KOH, and chloroplatinic acid hexahydrate (> 99%, H<sub>2</sub>PtCl<sub>6</sub>·H<sub>2</sub>O) were purchased from Aladdin Co. Ltd. The materials were all utilized without further purification and were all analytically pure. Deionized water was utilized throughout the experiments. Pure carbon quantum dots (CQDs) was prepared by citric acid according to a new method as shown in supplementary material.

### 2.2. Synthesis of bulk CN and alkali etching CN nanosheets

Bulk CN (CN (B)) was prepared from melamine according to a standard literature method. Briefly, 20 g of melamine was annealed at 550 °C in a muffle furnace for 4 h accompanied by a heating rate of 10 °C min<sup>-1</sup>. Different conjugated systems of CN nanosheets were synthesized as follows: 6 g of pristine CN (B) was dissolved in KOH aqueous solution with vigorous stirring (The mass ratio of CN (B): KOH respectively is 1: 1, 1: 2, and 1: 3 in 50 mL H<sub>2</sub>O), and then the resulting solution evaporated to dryness in an oven at 80 °C overnight. The solid mixtures of pristine CN (B) and KOH were then calcined at 300 °C in a muffle furnace for 1 h accompanied by a heating rate of 2 °C min<sup>-1</sup>. The obtained products were denoted as CN 3(x) (where x = 1, 2, and 3 and corresponds to the mass ratios (g) of KOH used). CN (2) was obtained by the same procedure using pristine CN (B) and KOH (mass ratio 1: 2) as precursor except for no heating process. Following synthesis, all samples were washed with HCl solution (0.1 M) and water to remove any residual alkali. The opaque powder was dried for 12 h at 80 °C in a vacuum drying oven.

### 2.3. Characterization

To characterize the structural variation of the materials, X-ray

diffraction (XRD) patterns (Bruker D8 Advance) were obtained using graphite monochromatized Cu-K $\alpha$  ( $\lambda$  = 1.5406 Å) radiation in the 2 $\theta$  range from 5° to 80°. Fourier transform infrared (FTIR) spectra of the materials were measured on a Bruker Tensor 27 spectrometer with the KBr tableting method. The Brunauer-Emmett-Teller (BET) specific surface area was determined by a surface area and porosity analyzer (ASAP 2020, American) based on nitrogen adsorption and desorption isotherms measured at 77 K. The degasification temperature and the drying time of the samples were 200 °C and 2 h, respectively. Microstructural characterization and the elemental mapping of desired regions were performed by field-emission scanning electron microscopy (FESEM, Hitachi, S-4800) and energy-dispersive X-Ray spectroscopy (EDS), respectively. Transmission electron microscopy (TEM) images were collected on an FEI Tecnai G2 F20 TEM. The UV-vis diffuse reflectance spectra (DRS, Hitachi U-3010 spectrophotometer) were obtained by the Kubelka-Munk approach with BaSO<sub>4</sub> as a reference at room temperature. X-ray photoelectron spectroscopy (XPS, Axis Ultra DLD, Kratos) measurements were carried out with a monochromatic X-ray source (Al K $\alpha$ , 15 kV, 200 W). Steady-state/time-resolved photoluminescence emission spectra (320 nm excitation) were measured at room temperature with a fluorescence spectrophotometer (Edinburgh Instruments, FLSP-920).

### 2.4. Photocatalytic water splitting

Photocatalytic experiments for H<sub>2</sub> evolution were carried out in a Pyrex reaction cell connected to a closed gas evacuation and circulation system. The composites (0.010 g) were sonicated for 5 min in a 78 mL triethanolamine aqueous solution (10 vol% TEOA, sacrificial reagent). The deposition of 2 wt% Pt as a reducing co-catalyst was achieved by dissolving H<sub>2</sub>PtCl<sub>6</sub> in the above 78 mL reaction solution. Then the aqueous suspension was degassed for 1 h and irradiated by a 300 W Xe lamp with an ultraviolet cut-off filter ( $\lambda$  > 420 nm) (PLS-SXE300, Trusttech). A flow of cooling water was used to maintain the reaction temperature at room temperature. The content of H<sub>2</sub> generated was determined by online gas chromatography (GC7900, Tian Mei, Shanghai) equipped with a 5 Å molecular sieve column and a thermal conductivity detector (TCD) using nitrogen as the carrier gas. In the case of the same other conditions, photocatalytic experiments for H<sub>2</sub> and O<sub>2</sub> evolution of photocatalysts were carried out in the pure water without using any sacrifice agent. The content of H<sub>2</sub> and O<sub>2</sub> generated was determined by online gas chromatography (GC7900, Tian Mei, Shanghai) equipped with a 5 Å molecular sieve column and a thermal conductivity detector (TCD) using argon as the carrier gas, as shown in Fig. S1.

### 2.5. Photoelectrochemical measurements

The electrochemical measurements (CHI660C, Electrochemical Instruments) utilized a standard three-electrode system with Na<sub>2</sub>SO<sub>4</sub> (1 mol L<sup>-1</sup>) aqueous solution as the electrolyte. Ag/AgCl (saturated KCl) and platinum flake were used as the reference electrodes and counter electrodes, respectively. The sample electrodes separately served as the working electrode, which was obtained by using the doctor blade coating method to deposit the suspensions onto indium tin oxide (ITO). The visible light source was a 300 W Xe lamp with an ultraviolet cut-off filter ( $\lambda$  > 420 nm) (PLS-SXE300, Trusttech). The working electrodes were prepared as follows: the nanocomposite (0.05 g) was ground with 0.5 mL deionized water and 0.02 g polyethylene glycol to make a slurry. Next, the slurry was coated onto ITO glass electrodes and these electrolytes were dried at 120 °C for 2 h.

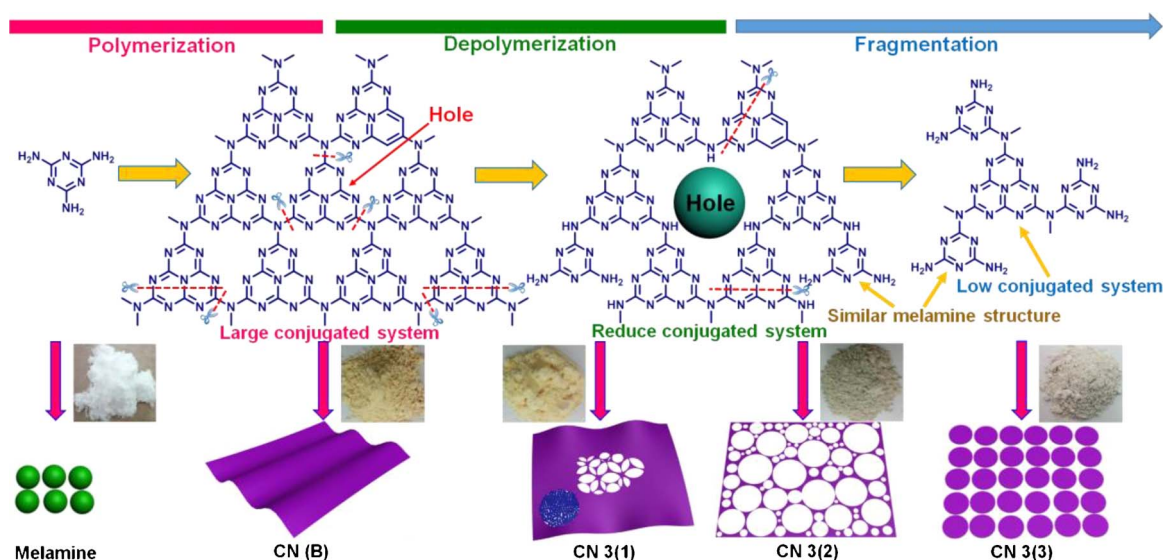


Fig. 1. Schematic illustration of the alkali depolymerization method to form holey graphitic carbon nitride nanosheets with tunable conjugated system.

### 3. Results and discussion

#### 3.1. Structure and composition

The critical component of the post-processing method is the alkali in which the CN (B) is heated to 300 °C for 1 h in the air atmosphere as shown in Fig. 1 and Fig. S2. It should be noted that the appropriate conjugated system with the suitable  $\pi$ - $\pi$  conjugated electronic system, optical performance, and the concentration and diameter of in-plane holes were obtained in the CN 3(2), depend crucially on the amount of alkali and the heating temperature (Fig. S3). The optimized mass ratio (CN (B): KOH) for preparing the suitable conjugated system of holey CN nanosheet is 1: 2. As shown in Fig. 2, the crystal structure of as-obtained samples was examined by evaluating their respective x-ray powder diffraction (XRD) patterns. The similar diffraction peaks of (100) and (002) were found to correspond the in-plane structural packing motif and the interlayer stacking of aromatic segments, respectively [33]. The similar diffraction peaks of (100) and (002) demonstrate that the main chemical skeleton of the as-obtained samples is well-maintained after the alkali treatment. However, the reduction in  $2\theta$  values shows the expansion of the interlayer distance based on Bragg's Law [34]. This

may be because the  $\pi$ - $\pi$  conjugated electronic system has reduced the  $\pi$ - $\pi$  interaction by the process of alkali depolymerization of g-C<sub>3</sub>N<sub>4</sub>, which disturbs the stacked layered structure. Furthermore, with increasing amount of alkali, the enlarged view of (002) diffraction peaks display a new peak that is consistent with the peak of pure melamine and which is absent in the XRD results of CN (B). These XRD results indicate that the  $\pi$ - $\pi$  conjugated electronic system of CN 3(3) may be closer to that of melamine. In addition, the Fourier transform infrared (FTIR) spectra further confirm the gradual reduction of the conjugated system of CN (B) to be closer to that of melamine. The FTIR spectra of melamine, CN (B), CN (2), CN 3(1), CN 3(2), and CN 3(3) samples (Fig. 3) exhibited different peaks at 810 cm<sup>-1</sup>, which can be ascribed to the deformation of the tri-s-triazine ring modes. Another peak at 1200–1700 cm<sup>-1</sup> was ascribed to the characteristic stretching modes in CN heterocycles. The peak at 2900–3600 cm<sup>-1</sup> was ascribed to water or amine groups [35–37]. However, after alkali treatment, the pattern of the FTIR spectra gradually approached that of melamine, indicating that the  $\pi$ - $\pi$  conjugated electronic system was progressively reduced by the alkali depolymerization process. More evidence supporting this conclusion could also be found in the results from transmission electron microscopy (TEM) and ultraviolet-visible diffuse reflectance spectra (UV-vis

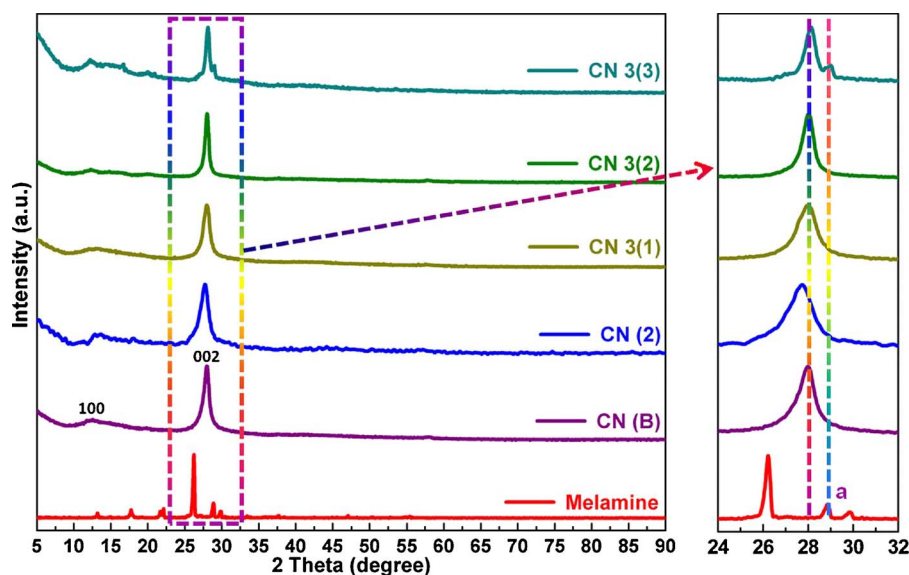


Fig. 2. XRD patterns of melamine, CN (B), CN (2), CN 3(1), CN 3(2), and CN 3(3) samples.



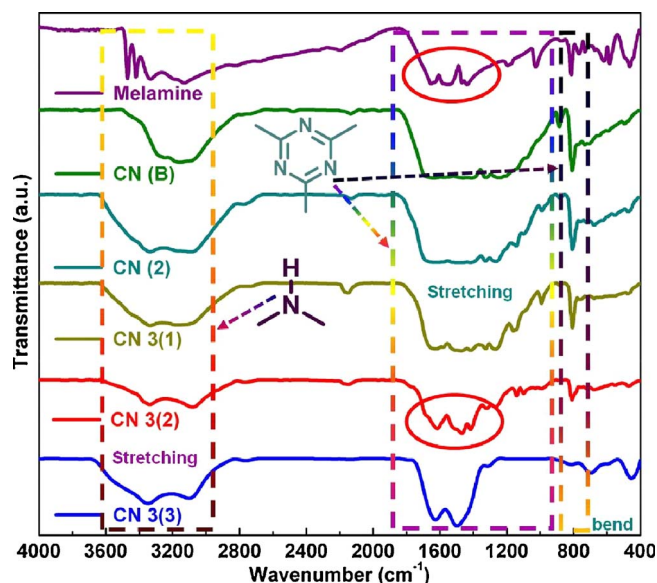


Fig. 3. Fourier transform infrared spectra of melamine, CN (B), CN (2), CN 3(1), CN 3(2), and CN 3(3) samples.

DRS).

To further investigate the effects of KOH treatment on the bulk CN and surface elemental valence states of the obtained photocatalysts, X-ray photoelectron spectroscopy (XPS) measurements were executed.

High-resolution XPS spectra (Fig. 4(a)) gave C 1s and N 1s core electron peaks of CN (B), CN 3(1), CN 3(2), and CN 3(3). As expected, the C 1s was decomposed at three peaks (Fig. 4(b)). The peaks at 288.0, 286.2, and 284.6 eV in high-resolution C 1s of CN (B) sample could be attributed to the  $sp^2$ -hybridized carbon in the N containing aromatic ring, the  $sp^2$ C atoms in the aromatic ring attached to the  $-NH_2$  group, and the standard reference carbon or  $sp^2$ -hybridized carbon, respectively [38]. Meanwhile, as shown in Fig. 4(c), the value of  $sp^2$ -hybridized N in the C=N–C groups, tertiary nitrogen N–(C)<sub>3</sub>, and the N–H bond of melon peaked at 398.6, 400.3, and 404.3 eV, respectively [39]. In comparison with the CN (B), the binding energies of N 1s and C 1s electrons of CN 3(1), CN 3(2), and CN 3(3) showed small variations due to the redistribution of charge in the CN nanosheets with the modified  $\pi$ - $\pi$  conjugated electronic system and C/N atomic ratio. Elemental analysis (Table S1) revealed that CN 3(1), CN 3(2), and CN 3(3) have smaller C/N atomic ratios (0.69, 0.64, and 0.52) than that of CN (B) (0.71), as approximated by the atomic ratio of the stoichiometric carbon nitride (0.75). As is known, the residual amine groups ( $NH_2/NH$ ) are in charge of the taller density of nitrogen in the ordinarily available g- $C_3N_4$  [40]. In addition, as compared to the N(C<sub>3</sub>) and N(C<sub>2</sub>) groups, the nitrogen in the amine groups is easily lost by theoretical prediction [41]. Therefore, the gradually decreased C: N atomic ratio could be reduced the loss of the amine groups in the formation process of CN 3(1), CN 3(2), and CN 3(3).

The in-plane holes will not only significantly impede their aggregation by extremely decreasing interaction locations but also effectively enhance the number of uncovered active locations. Therefore, the specific surface area and pore structure of the CN (B) and CN 3(2) are

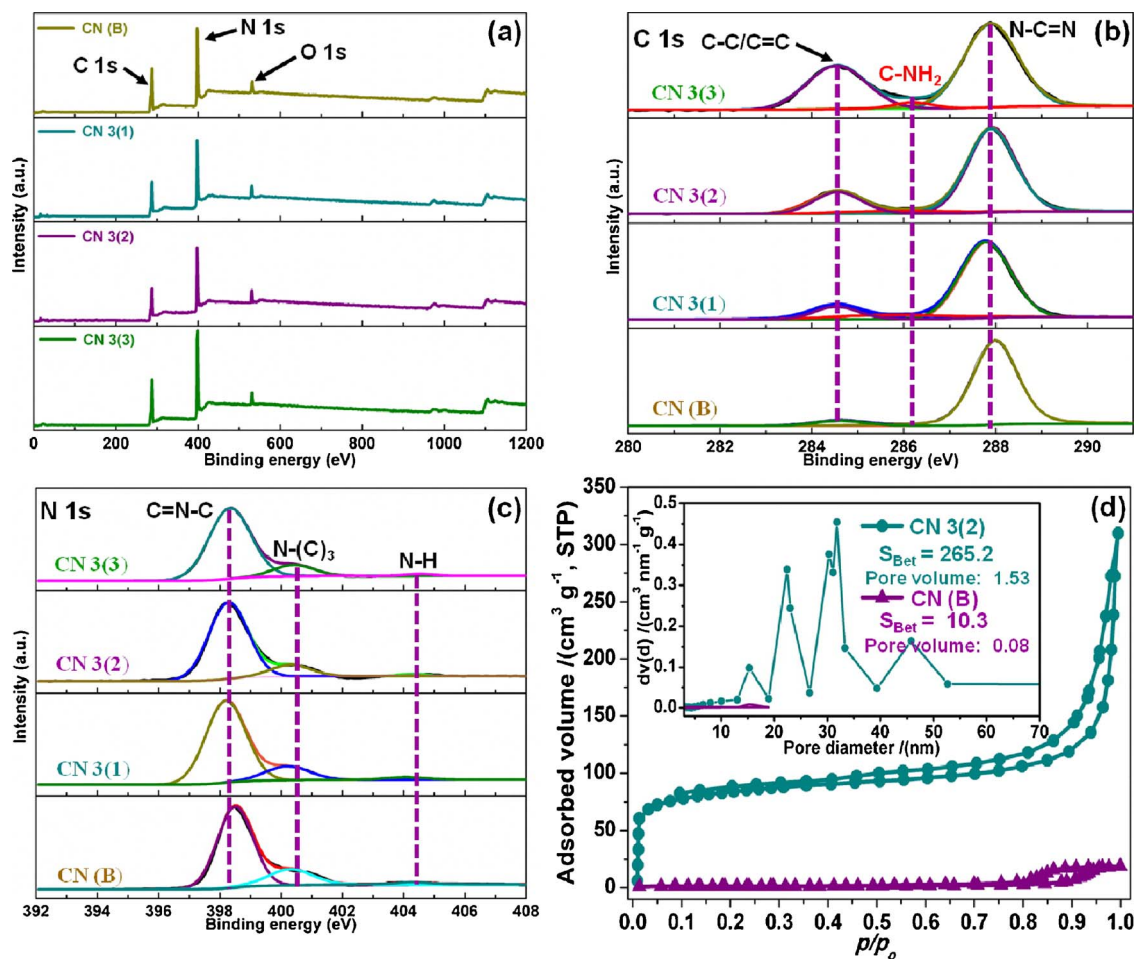
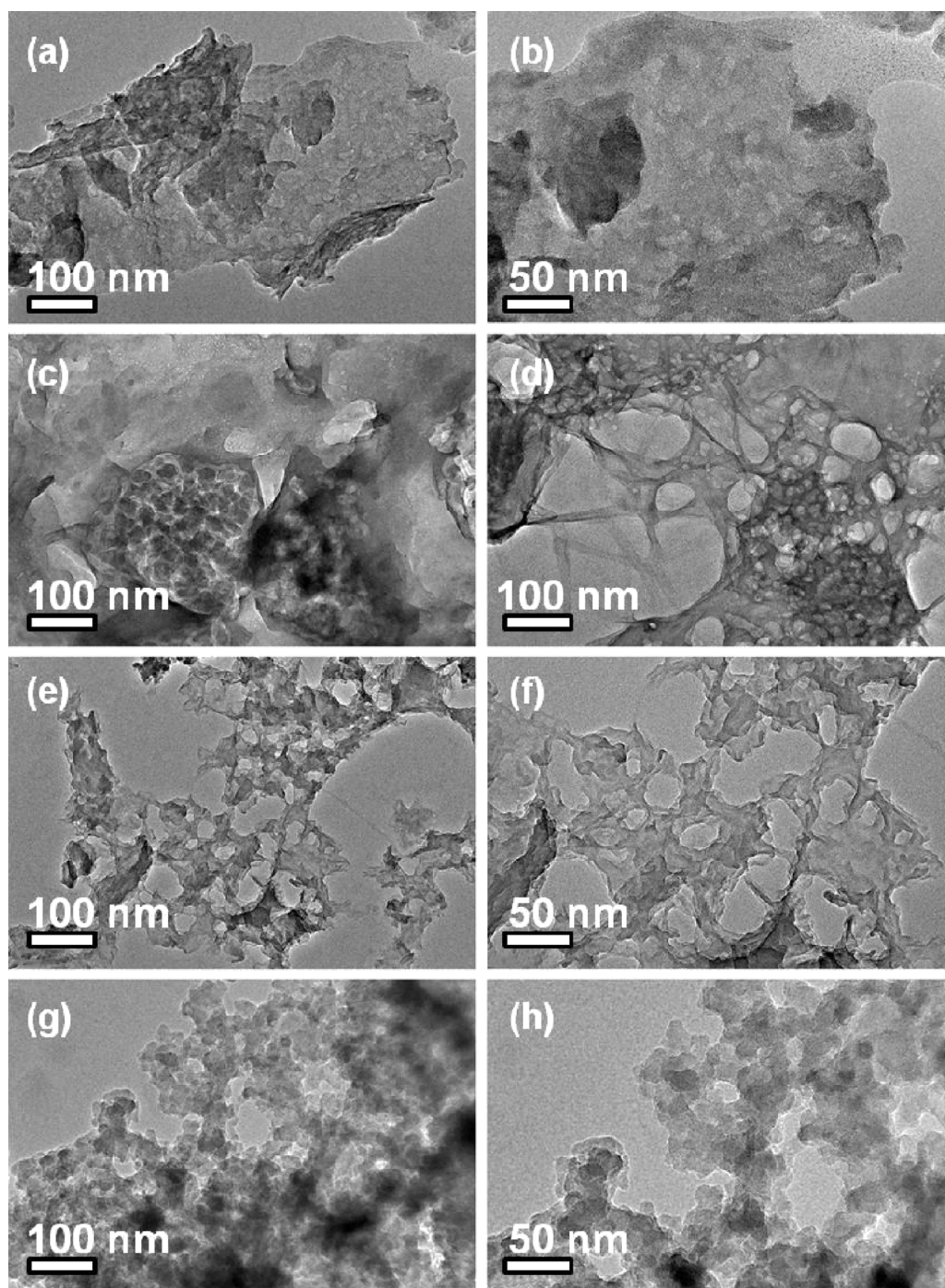


Fig. 4. (a) XPS survey spectra of CN (B), CN 3(1), CN 3(2), and CN 3(3) samples. (b) C 1s and (c) N 1s of the materials. (d)  $N_2$  adsorption-desorption isotherms at 77 K and the corresponding pore size distribution (PSD) curves (inset) of CN (B) and CN 3(2) samples.



**Fig. 5.** TEM images of ((a), (b)) CN (B), ((c), (d)) CN 3(1), ((e), (f)) CN 3(2), and ((g), (h)) CN 3(3) samples.

characterized by the specific surface area and porosity analyzer. As shown in Fig. 4(d), the existence of plentiful mesopores and macropores of CN 3(2) are obtained from a type-IV isotherm. The specific surface area of CN (G/S) ( $\approx 265.2 \text{ m}^2 \text{ g}^{-1}$ ) is 25.7 times higher than that of CN (B) ( $\approx 10.3 \text{ m}^2 \text{ g}^{-1}$ ). Correspondingly, compared to CN (B), CN 3(2) occupies a very high pore volume. The total pore volume of CN (G/S) ( $\approx 1.53 \text{ cm}^3 \text{ g}^{-1}$ ) is 19.1 times higher than that of CN (B) ( $\approx 0.08 \text{ cm}^3 \text{ g}^{-1}$ ). It is never reported that the total pore volume of nanostructured CN materials has exhibited such a high value [42,43]. Many of the crumpled and in-plane hole structures are resulted from an extremely high pore volume. Through using the Barrett-Joyner-Halenda method, the pore size distribution plots were further characterized the pore structure of CN 3(2). The pore size distribution curve of CN (B) shows negligible peaks. On the contrary, the pore size distribution

curve of CN 3(2) has a strong peak at about 30 nm and a lenient distribution in the scope of 20–60 nm. Compared with the same weight as CN (B), the large pore volume and high specific surface area lead to a much larger volume of CN 3(2), which may obviously enhance the kinetics ability of overall water splitting by accelerating charge separation and transfer [44].

Scanning electron microscope (SEM) images illustrate that the pristine CN (B) was extensively agglomerated and had a smooth surface (Fig. S4(a<sub>1</sub>) and (a<sub>2</sub>)). The bulky structure obstructed its capabilities of light absorption, charge and mass transport [45]. After alkali treatment, the CN 3(1) sample did not change its morphological features, but the microscopic surface showed many in-plane holes (Fig. S4(b<sub>1</sub>) and (b<sub>2</sub>)). Furthermore, with gradual increase in the amount of alkali, CN 3(2) and CN 3(3), respectively, showed a smaller size of the 2D layer (Fig.



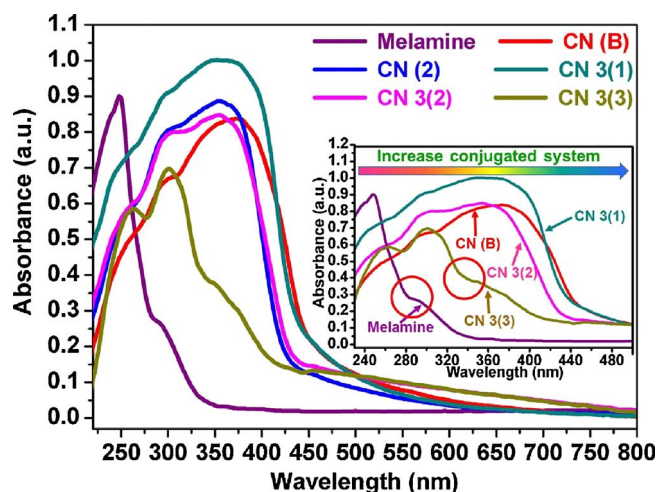


Fig. 6. UV-vis diffuse reflectance spectra (DRS) of melamine, CN (B), CN (2), CN 3(1), CN 3(2), and CN 3(3) samples.

S4(c<sub>1</sub>) and (c<sub>2</sub>)) and a very small size of the nanosheet (Fig. S4(d<sub>1</sub>) and (d<sub>2</sub>)). The energy dispersive X-ray spectroscopy (EDS) investigations (Fig. S5) revealed the presence of C and N with no other impurity elements. The EDS signal was obtained from the SEM.

The TEM results of CN (B) revealed overlapping and large-size 2D nanosheets (Fig. 5(a) and (b)). With the addition of alkali, a reduced sheet size and some in-plane holes all appeared in the overlapping and large-size 2D nanosheets of CN 3(1) (Fig. 5(c) and (d)). With further increase in the amount of alkali, a large quantity of the opened pores having dozens of nanometers diameter in the CN 3(2) were evident (Fig. 5(e) and (f)). The formation mechanism of holey structure in the CN 3(2) could be that alkali etch the N=C=N, C-NH<sub>2</sub>, and C=C lattice sites of CN (B), resulting in carbon vacancy, thus forming a holey structure. However, compared to CN (B) sample with the large-size 2D nanosheets, the size of the 2D nanosheets of CN 3(3) was very small (Fig. 5(g) and (h)). This fact is intuitive proof that the conjugated system of g-C<sub>3</sub>N<sub>4</sub> was gradually reduced by the alkali treatment method. More importantly, it was noted that the conjugated system of the g-C<sub>3</sub>N<sub>4</sub> sample was regulated for the first time by facile alkali etching method.

### 3.2. Optical property

It is expected that the distinct  $\pi$ - $\pi$  conjugated electronic system of holey 2D nanosheets would have a strong impact on the optical performances of CN materials. The optical properties of the CN nanosheets were studied by recording the UV-vis DRS. Fig. 6 indicates that, in comparison with that of melamine, a great red shift of the intrinsic absorption edge of CN (B) due to an ordinary thermal polymerization process was evident. By contrast, in comparison with that of CN (B), a gradual blue shift of the intrinsic absorption edge of the different conjugated system of the alkali treated CN nanosheets was observed. This shift can be attributed to the well-known quantum confinement effect with the different  $\pi$ - $\pi$  conjugated electronic system [46]. Furthermore, the pattern of the absorbance curve of CN 3(3) is like that of melamine. These results thus indicate that the conjugated system of the g-C<sub>3</sub>N<sub>4</sub> sample was successfully regulated by the facile alkali etching method. Furthermore, based on the plot of transformed Kubelka-Munk function  $(ah\nu)^{1/2}$  versus the energy of exciting light  $(h\nu)$  (Fig. S6), the band-gaps of melamine, CN (B), CN (2), CN 3(1), CN 3(2), and CN 3(3) were estimated to be 3.48, 2.55, 2.73, 2.58, 2.66, and 3.18 eV, respectively. By linearly extrapolating the leading edge of the valence band (VB) of the XPS of CN (B), CN 3(1), CN 3(2), and CN 3(3) to the base line (Fig. S7), the VB level were respectively determined to be +1.88, +1.86, +1.70, and +2.62 eV [47]. The band-gap of CN (B), CN 3(1), CN 3(2), and CN 3(3) were respectively determined to be 2.55, 2.58, 2.66, and 3.18 eV, with the corresponding CB position at -0.67, -0.72, -0.96, and -0.56 eV (Fig. 7). In comparison with CN (B), the CB potential of CN 3(2) upshifted by about 0.29 eV, which may have led to the larger thermodynamic driving force during the photocatalytic hydrogen production. However, in comparison with CN (B), the CB potential of CN 3(3) downshifted by about 0.11 eV, which may be led to the low thermodynamic driving force during the photocatalytic hydrogen evolution. This indicates that the appropriate conjugated system of CN nanosheet is important for reducing the serious aggregation and stacked layered structure and preserving the proper band gap. The band structure indicates that the band edge of CN nanosheets well satisfies the thermodynamic requirement for water oxidation-reduction reaction [48].

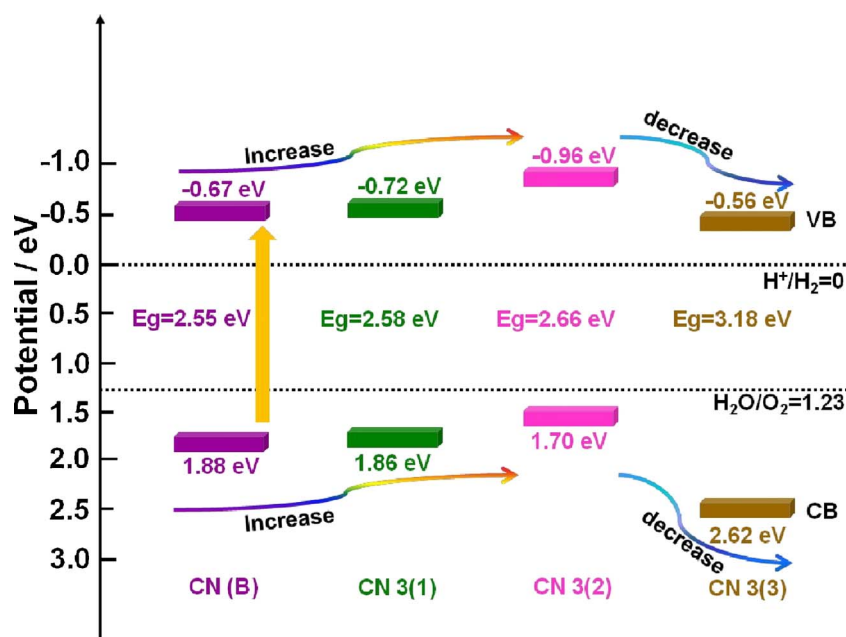


Fig. 7. Band structure alignments for pristine CN (B), CN 3(1), CN 3(2), and CN 3(3) samples.

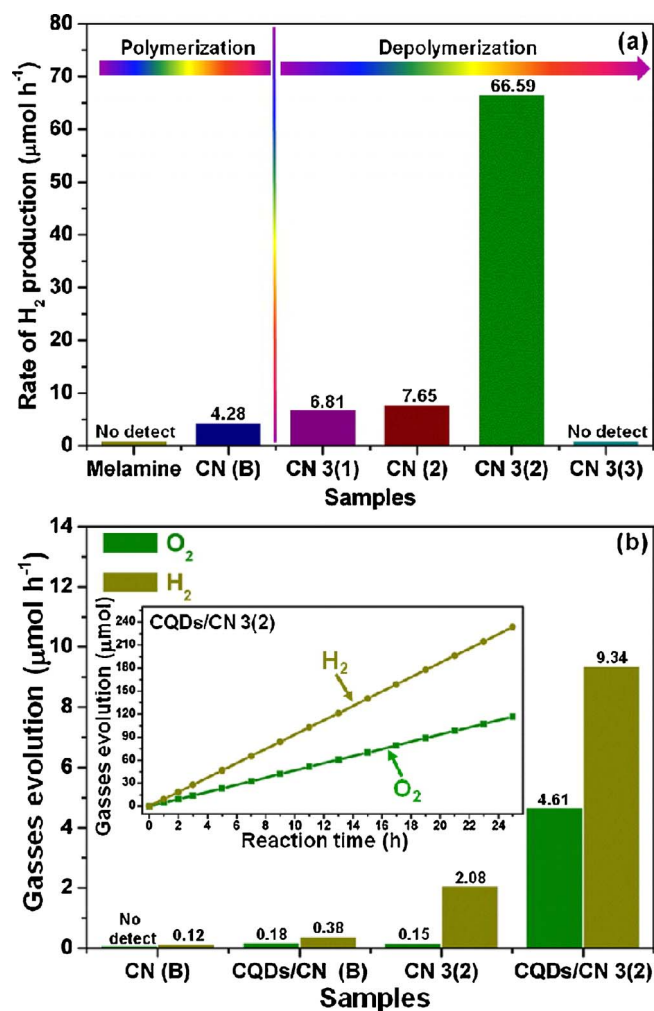


Fig. 8. (a) Photocatalytic activity of the investigated samples in an aqueous solution containing 10 vol% TEOA with added 2 wt% Pt (H<sub>2</sub>PtCl<sub>6</sub>) under visible light irradiation. (b) Photocatalytic activity of CN (B) and CN 3(2) samples in an aqueous solution containing 70 mL H<sub>2</sub>O with added 2 wt% Pt (H<sub>2</sub>PtCl<sub>6</sub>) under visible light irradiation. Furthermore, H<sub>2</sub> and O<sub>2</sub> generation of CQDs/CN (B) and CQDs/CN 3(2) from 70 mL water with added 2 wt% Pt (H<sub>2</sub>PtCl<sub>6</sub>) under visible light irradiation.

### 3.3. Photocatalytic water splitting and stability

The photocatalytic H<sub>2</sub> evolution abilities of melamine, CN (B), CN (2), CN 3(1), CN 3(2), and CN 3(3) were each investigated using an aqueous solution of 10 vol% triethanolamine (TEOA) with 2 wt% Pt (H<sub>2</sub>PtCl<sub>6</sub>) added, under irradiation with visible light ( $\lambda > 420$  nm). As shown in Fig. 8(a), the rates of the visible-light-driven photocatalytic H<sub>2</sub> evolution from melamine, CN (B), CN (2), CN 3(1), CN 3(2), and CN 3(3) were no detect, 4.28, 6.81, 7.65, 66.59, and no detect  $\mu\text{mol h}^{-1}$ , respectively. The H<sub>2</sub> production rate of CN 3(2) was almost 15.6 times greater than that of CN (B). However, the H<sub>2</sub> production rate of melamine and CN 3(3) were not detectable. Hence, these different photocatalytic H<sub>2</sub> evolution activities shown by CN nanosheets may be due to the resulting from the different conjugated systems that arise from the different band gaps. To further verify the photocatalytic performance, assessment of the overall water splitting performance of both CN (B) and CN 3(2) was performed using pure water under visible light irradiation (Fig. 8(b)). Pt (2 wt%) was photo-loaded in situ onto different CN nanosheets as a co-catalyst to boost H<sub>2</sub> generation. The H<sub>2</sub> and O<sub>2</sub> production rate of CN (B) were respectively 0.12  $\mu\text{mol h}^{-1}$  and no detect. Meanwhile, the H<sub>2</sub> and O<sub>2</sub> production rate of CN 3(2) were 2.08 and 0.15  $\mu\text{mol h}^{-1}$ , respectively. The H<sub>2</sub> production rate of CN 3(2) was 17.3 times greater than that of CN (B). As is known, photocatalytic

water splitting to O<sub>2</sub> and H<sub>2</sub> demands a high free energy of 113.38 kcal/mol [49,50]. Compared with the two-electron process for H<sub>2</sub>O<sub>2</sub> formation (1.78 eV), the concerted four-electron process for oxygen evolution (1.23 eV) has obvious thermodynamic advantages [51]. Unfortunately, reported results show that a higher reactivity may be obtained in a photocatalyst where pure water is first oxidized to H<sub>2</sub> and H<sub>2</sub>O<sub>2</sub> by a two-electron reaction, followed by H<sub>2</sub>O<sub>2</sub> disintegration to H<sub>2</sub>O and O<sub>2</sub> [52]. According to published literature [53,54], carbon quantum dots (CQDs) can have high catalytic activity for H<sub>2</sub>O<sub>2</sub> disintegration as they do not require light and exhibit chemical catalysis. High-resolution TEM (HRTEM) image (Fig. S8(a) and (b)) present the (002) plane of CQDs that have an inherent spacing distance of 0.32 nm [55,56]. A size distribution shows that the spherical nanoparticles are distributed evenly with an average particle size of  $1.7 \pm 0.9$  nm (Fig. S8(c)). The particle size of CQDs is mostly 1.5–1.9 nm. Fig. 8(b) shows the production of H<sub>2</sub> and O<sub>2</sub> from 70 mL of pure water with 0.010 g of non-optimized CQDs/CN (B) and CQDs/CN 3(2) samples under irradiation with visible light. H<sub>2</sub> and O<sub>2</sub> were quantified through online gas chromatography; a gas chromatography (GC) signal of the representative composite curve is shown in Fig. S9. The H<sub>2</sub> and O<sub>2</sub> evolution rates of the CQDs/CN (B) were 0.38 and 0.18  $\mu\text{mol h}^{-1}$ , respectively. Meanwhile, the H<sub>2</sub> and O<sub>2</sub> evolution rates of the CQDs/CN 3(2) were 9.34 and 4.61  $\mu\text{mol h}^{-1}$ , respectively. The CN 3(2) had a much higher photocatalytic H<sub>2</sub> and O<sub>2</sub> evolution rate of about 24.6 times that of CN (B). Furthermore, no other gasses that O<sub>2</sub> and H<sub>2</sub> (e.g., N<sub>2</sub> or CO<sub>2</sub>) were detected by online gas chromatography. H<sub>2</sub> and O<sub>2</sub> evolution of CQDs/CN 3(2) always resulted in an H<sub>2</sub>/O<sub>2</sub> molar ratio of 2.03, which is consistent with the theoretical value of 2 for photocatalytic water splitting. The apparent quantum efficiency (AQE) for CN 3(2) with the addition of 10 vol% TEOA aqueous solution reached 12.1% at 420 nm. A photocatalyst must display repeatable performance for its successful practical application [57]. The repeatability of CN 3(2) performance was assessed under visible light irradiation by carrying through a “time-circle” H<sub>2</sub> production in seven consecutive runs that totaled 28 h. As shown in Fig. 9(a), it exhibited remarkable stability and little deactivation of the photocatalyst occurred upon repeated use. In addition, analysis of the FTIR spectra, XRD patterns, and TEM of CN (G/T) after this experiment (Fig. S10 and S11) also indicated its good stability [58].

### 3.4. Clarification of the mechanism

The photo-luminescence (PL) spectroscopy technique can be considered as useful method to comprehend the transfer and recombination of the photo-induced electron-hole in a composite [59]. Thus, the PL spectra of as-obtained photocatalysts have been investigated as shown in Fig. 9(b). The PL spectrum of pure CN (B) displayed a platform emission peak at 450 nm due to the band-to-band recombination of electron-hole. The intensity of the emission bands of CN 3(2) and CN 3(1) were lower than that of CN (B), demonstrating that the recombination of photo-generated electron-hole pairs through unique conjugated system was more suppressed for CN 3(1) and CN 3(2) than that for CN (B). In addition, the emission peak undergoes a progressive blue-shift from the 450 nm associated with pure CN (B) to around 426 nm resulting from the transfer of the absorption edge toward lower wavelengths. In general, this happens in the presence of a suitable  $\pi$ - $\pi$  conjugated electronic system, which was found to be beneficial for the migration of photo-generated electrons, thereupon restricting the recombination of photo-produced electron-hole. Moreover, two trap states with different trap depths were associated with the recovery featuring two decay components. In other words, photo-generated electrons in the conduction band are transmitted from a shallow-trap state to a deep-trap state [60,61]. Time-resolved photoluminescence (PL) spectra of CN (B), CN 3(1), and CN 3(2) were obtained to judge whether they would have such trap states with long lifetimes (Fig. 9(c)). The acquired PL lifetimes for CN (B), CN 3(1), and CN 3(2) were 5.59,

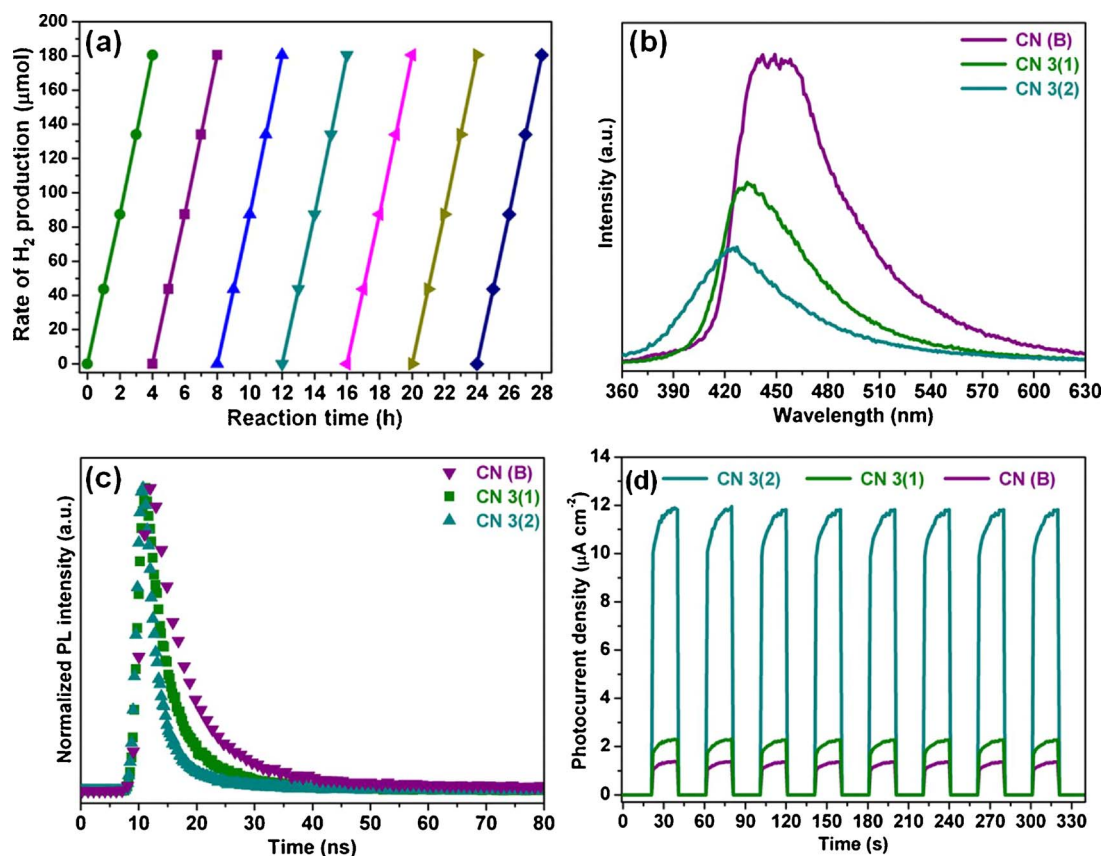


Fig. 9. (a) Cycling test of photocatalytic H<sub>2</sub> generation for CN 3(2) with no addition of a sacrificial agent in the photocatalytic experiment period (the reaction was repeated every 4 h. An experimental vacuum apparatus was used). (b) Steady-state photoluminescence (PL) spectra of CN (B), CN 3(1), and CN 3(2). (c) Time-resolved PL decay profiles for CN (B), CN 3(1), and CN 3(2). (d) Transient photocurrent responses of CN (B), CN 3(1), and CN 3(2) in 1 mol L<sup>-1</sup> aqueous solution under irradiation with visible light.

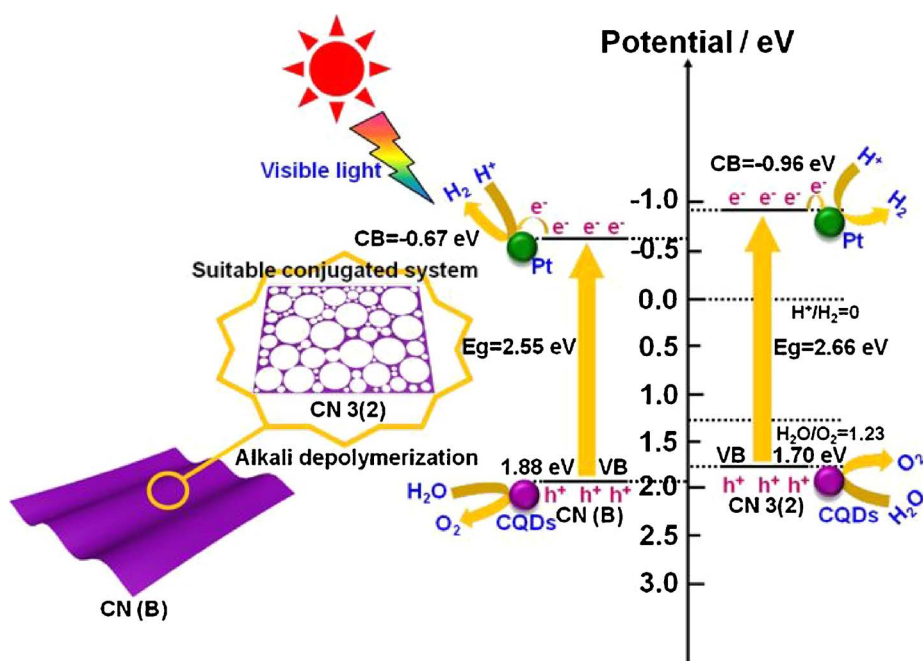


Fig. 10. A possible mechanism for the photocatalytic water splitting about CN (B) and CN 3(2), respectively.

4.51, and 3.78 ns, respectively. To further demonstrate the charge separation efficiency levels, the transient photocurrent responses of the as-synthesized photoelectrodes were obtained from the *I*-*t* curves with eight on-off cycles under visible light irradiation [62]. The photocurrent value was observed instantly at all the photoelectrodes when the lamp was turned on, and then quickly returned to zero when the

lamp was turned off, demonstrating that the photoelectrodes had great stability and repeatability (Fig. 9(d)). These results indicated that the order of the photocurrent value under irradiation by visible light was CN 3(2) > CN 3(1) > CN (B), which further confirmed that the CN 3(2) sample could greatly improve the separation of photo-produced electron-hole. This outcome was extremely consistent with the results



obtained from the PL spectra and the time-resolved PL spectra.

A probable mechanism expounding the activity of overall water splitting of CN (B) and CN 3(2) are respectively illustrated in Fig. 10. The oxidation level for H<sub>2</sub>O to H<sub>2</sub>O<sub>2</sub> or O<sub>2</sub> is above the valence band (VB), and the reduction level for H<sub>2</sub> is positioned below the conduction band (CB). These bands respectively are appropriately positioned to allow migration of holes and electrons for photocatalytic water splitting [63]. Thence, the potential of CN (B) and CN 3(2) is suitable as a photocatalyst for photocatalytic H<sub>2</sub> and O<sub>2</sub> evolution. Under visible light irradiation, the electrons in the VB of CN (B) and CN 3(2) were excited to its CB, and then transferred to Pt for protons reduction. Meantime, the holes in the VB of CN (B) and CN 3(2) were transferred to CQDs for oxidation reaction. Furthermore, the more negative CB level of CN (G/T) (−0.96 eV) than that of CN (B) (−0.67 eV) enhanced the reduction ability of CN (G/T). Obviously, through adjusting the conjugated system, the holey CN nanosheet improved the separation and transmission efficiency of photo-induced electron (e<sup>−</sup>)-hole (h<sup>+</sup>) pairs.

#### 4. Conclusions

In summary, a method of gradual depolymerization was designed meticulously to realize the conversion of the large conjugated system of CN (B) to the low conjugated system of CN 3(3), which is close to the conjugated system of pure melamine. The holey CN nanosheet with tunable conjugated system was fabricated by the alkali treatment of CN (B) in air. The alkali etching procedure is conducive to exfoliating the CN (B) into nanosheets with a suitable conjugated system and produces plentiful in-plane holes with carbon vacancies, resulting in large specific surface area without apparently affecting the optical performance. Compared to CN (B), CN 3(2) exhibited an approximately 24.6 times higher photocatalytic water splitting activity under irradiation of visible light, owing to the suitable  $\pi$ - $\pi$  conjugated electronic system, a larger accessible specific surface area, its holey structure, better light absorption, and a tremendously enhanced separation efficiency of photo-induced electron and hole. This study demonstrated a straightforward and environmentally-friendly strategy to design highly-efficient graphitic carbon nitride photocatalysts for potential application in solar-energy-driven photocatalytic water splitting.

#### Acknowledgements

We are extremely grateful to the research fund of the Key Laboratory of Fuel Cell Technology of Guangdong Province and the National Natural Science Foundation of China (No. 21571064, 21371060) for financial support.

#### Appendix A. Supplementary data

Supplementary data associated with this article can be found, in the online version, at <http://dx.doi.org/10.1016/j.apcatb.2017.11.039>.

#### References

- [1] J. Ran, J. Zhang, J. Yu, M. Jaroniec, S.Z. Qiao, *Chem. Soc. Rev.* 43 (2014) 7787–7812.
- [2] M.A. Shannon, P.W. Bohn, M. Elimelech, J.G. Georgiadis, B.J. Marinas, A.M. Mayes, *Nature* 452 (2008) 301–310.
- [3] P. Zhou, J.G. Yu, M. Jaroniec, *Adv. Mater.* 26 (2014) 4920–4935.
- [4] T. Hisatomi, J. Kubota, K. Domen, *Chem. Soc. Rev.* 43 (2014) 7520–7535.
- [5] J.R. Ran, T.Y. Ma, G.P. Gao, X.W. Du, S.Z. Qiao, *Energy Environ. Sci.* 8 (2015) 3708–3717.
- [6] Y. Zheng, L. Lin, B. Wang, X. Wang, *Angew. Chem. Int. Ed.* 54 (2015) 12868–12884.
- [7] Y. Kim, D. Shin, W.J. Chang, H.L. Jang, C.W. Lee, H.E. Lee, K.T. Nam, *Adv. Funct. Mater.* 25 (2015) 2369–2377.
- [8] S. Cao, J. Low, J. Yu, M. Jaroniec, *Adv. Mater.* 27 (2015) 2150–2176.
- [9] C. Chang, L.Y. Zhu, S.F. Wang, X.L. Chu, L.F. Yue, *ACS Appl. Mater. Interfaces* 6 (2014) 5083–5093.
- [10] X.C. Wang, K. Maeda, A. Thomas, K. Takanabe, G. Xin, J.M. Carlsson, K. Domen, M. Antonietti, *Nat. Mater.* 8 (2009) 76–80.
- [11] W. Yong, X.C. Wang, M. Antonietti, *Angew. Chem. Int. Ed.* 51 (2012) 68–89.
- [12] J. Zhang, M. Zhang, L. Lin, X. Wang, *Angew. Chem. Int. Ed.* 21 (2015) 6297–6301.
- [13] J.S. Zhang, J.H. Sun, K. Maeda, K. Domen, P. Liu, M. Antonietti, X.Z. Fu, X.C. Wang, *Energy Environ. Sci.* 4 (2011) 675–678.
- [14] P. Niu, G. Liu, H.M. Cheng, *J. Phys. Chem. C* 116 (2012) 11013–11018.
- [15] H. Li, J. Liu, W. Hou, N. Du, R. Zhang, X. Tao, *Appl. Catal. B: Environ.* 160 (2014) 89–97.
- [16] X. Zhang, L. Yu, C. Zhuang, T. Peng, R. Li, X. Li, *ACS Catal.* 4 (2013) 162–170.
- [17] X. Zhang, X. Xie, H. Wang, J. Zhang, B. Pan, Y. Xie, *J. Am. Chem. Soc.* 135 (2013) 18–21.
- [18] J.S. Xu, M. Antonietti, *J. Am. Chem. Soc.* 139 (2017) 6026–6029.
- [19] X.H. Li, X.C. Wang, M. Antonietti, *Chem. Sci.* 3 (2012) 2170–2174.
- [20] Q. Guo, Y. Xie, X. Wang, S. Zhang, T. Hou, S. Lv, *Chem. Commun.* 1 (2004) 26–27.
- [21] Y. Zhao, F. Zhao, X. Wang, C. Xu, Z. Zhang, G. Shi, L. Qu, *Angew. Chem. Int. Ed.* 53 (2014) 13934–13939.
- [22] D. Zheng, C. Huang, X. Wang, *Nanoscale* 7 (2015) 465–470.
- [23] Q. Han, B. Wang, Y. Zhao, C. Hu, L. Qu, *Angew. Chem. Int. Ed.* 54 (2015) 11433–11437.
- [24] Y.X. Zeng, C.B. Liu, L.L. Wang, S.Q. Zhang, Y.B. Ding, Y.Z. Xu, Y.T. Liu, S.L. Luo, *J. Mater. Chem. A* 4 (2016) 19003–19010.
- [25] S. Yang, Y. Gong, J. Zhang, L. Zhan, L. Ma, Z. Fang, R. Vajtai, X. Wang, P. Ajayan, *Adv. Mater.* 25 (2013) 2452–2456.
- [26] Q. Lin, L. Li, S. Liang, M. Liu, J. Bi, L. Wu, *Appl. Catal. B: Environ.* 163 (2015) 135–142.
- [27] H. Wang, Y. Su, H. Zhao, H. Yu, S. Chen, Y. Zhang, X. Quan, *Environ. Sci. Technol.* 48 (2014) 11984–11990.
- [28] J.J. Ji, J. Wen, Y.F. Shen, Y.Q. Lv, Y.L. Chen, S.Q. Liu, H.B. Ma, Y.J. Zhang, *J. Am. Chem. Soc.* 139 (2017) 11698–11701.
- [29] Y. Hou, J. Li, Z. Wen, S. Cui, C. Yuan, J. Chen, *Nano Energy* 8 (2014) 157–164.
- [30] Z.M. Pan, Y. Zheng, F.S. Guo, P.P. Niu, X.C. Wang, *ChemSusChem* 10 (2017) 87–90.
- [31] Y.F. Zhao, W. Ran, J. He, Y.F. Song, C.M. Zhang, D.B. Xiong, F.M. Gao, J.S. Wu, Y.Y. Xia, *ACS: Appl. Mater. Interfaces* 7 (2015) 1132–1139.
- [32] Q.H. Liang, Z. Li, Z.H. Huang, F.Y. Kang, Q.H. Yang, *Adv. Funct. Mater.* 25 (2015) 6885–6892.
- [33] F. He, G. Chen, Y. Yu, Y. Zhou, Y. Zheng, S. Hao, *Chem. Commun.* 51 (2015) 6824–6827.
- [34] Y. Zhou, L. Zhang, W. Huang, Q. Kong, X. Fan, M. Wang, J. Shi, *Carbon* 99 (2016) 111–117.
- [35] J.Y. Liu, H. Xu, Y.G. Xu, Y.H. Song, J.B. Lian, Y. Zhao, L. Wang, L.Y. Huang, H.Y. Ji, H.M. Li, *Appl. Catal. B: Environ.* 207 (2017) 429–437.
- [36] Z. Zhao, Y. Sun, F. Dong, *Nanoscale* 7 (2015) 15–37.
- [37] X.J. She, J.J. Wu, J. Zhong, H. Xu, Y.C. Yang, R. Vajtai, J. Lou, Y. Liu, D.L. Du, H.M. Li, P.M. Ajayan, *Nano Energy* 27 (2016) 138–146.
- [38] W.J. Ong, L.L. Tan, S.P. Chai, S.T. Yong, A.R. Mohamed, *Nano Energy* 13 (2015) 757–770.
- [39] Y.F. Guo, J. Li, Y.P. Yuan, L. Li, M.Y. Zhang, C.Y. Zhou, Z.Q. Lin, *Angew. Chem. Int. Ed.* 55 (2016) 14693–14697.
- [40] B.V. Lotsch, M. Dobliger, J. Sehnert, L. Seyfarth, J. Senker, O. Oeckler, W. Schnick, *J. Chem. Eur.* 13 (2007) 4969–4980.
- [41] P. Niu, L.C. Yin, Y.Q. Yang, G. Liu, H.M. Cheng, *Adv. Mater.* 26 (2014) 8046–8052.
- [42] X. Jin, V.V. Balasubramanian, S.T. Selvan, D.P. Sawant, M.A. Chari, G.Q. Lu, A. Vinu, *Angew. Chem.* 121 (2009) 8024–8027.
- [43] Z. Zhao, Y. Dai, J. Lin, G. Wang, *Chem. Mater.* 26 (2014) 3151–3161.
- [44] P. Yang, J. Zhao, W. Qiao, L. Li, Z. Zhu, *Nanoscale* 7 (2015) 18887–18890.
- [45] T.R. Chetia, M.S. Ansari, M. Qureshi, *J. Mater. Chem. A* 4 (2016) 5528–5541.
- [46] P. Niu, L.L. Zhang, G. Liu, H.M. Cheng, *Adv. Funct. Mater.* 22 (2012) 4763–4770.
- [47] Y.F. Zhang, S.J. Park, *J. Catal.* 355 (2017) 1–10.
- [48] K. Zhang, L.Y. Wang, X.W. Sheng, M. Ma, M.S. Jung, W.J. Kim, H. Lee, J.H. Park, *Adv. Energy Mater.* 6 (2016) 1502352–1502359.
- [49] F. Rappaport, M.G. Kuras, P.J. Nixon, B.A. Diner, J. Lavergne, *Biochemistry* 41 (2002) 8518–8527.
- [50] G. Ananyev, G.C. Dismukes, *Photosynth. Res.* 84 (2005) 355–365.
- [51] J. Liu, Y. Liu, N.Y. Liu, Y.Z. Han, X. Zhang, H. Huang, Y. Lifshitz, S.T. Lee, J. Zhong, Z.H. Kang, *Science* 347 (2015) 970–974.
- [52] Y. Shiraishi, S. Kanazawa, Y. Sugano, D. Tsukamoto, H. Sakamoto, S. Ichikawa, T. Hirai, *ACS Catal.* 4 (2014) 774–780.
- [53] H.T. Li, Z.H. Kang, Y. Liu, S.T. Lee, *J. Mater. Chem.* 22 (2012) 24230–24253.
- [54] Y.F. Zhang, S.J. Park, *Carbon* 122 (2017) 287–297.
- [55] B.C.M. Martindale, G.A.M. Hutton, C.A. Caputo, E. Reisner, *J. Am. Chem. Soc.* 137 (2015) 6018–6025.
- [56] P.Y. Zhang, T. Song, T.T. Wang, H.P. Zeng, *Appl. Catal. B: Environ.* 206 (2017) 328–335.
- [57] T. Song, J.P. Huo, T. Liao, J. Zeng, J.Y. Qin, H.P. Zeng, *J. Chem. Eng.* 287 (2016) 359–366.
- [58] T. Song, L. Zhang, P.Y. Zhang, J. Zeng, T.T. Wang, A. Ali, H.P. Zeng, *J. Mater. Chem. A* 5 (2017) 6013–6018.
- [59] Y.P. Yuan, L.S. Yin, S.W. Cao, G.S. Xu, C.H. Li, C. Xue, *Appl. Catal. B: Environ.* 168 (2015) 572–576.
- [60] R. Wang, L.N. Gu, J.J. Zhou, X.L. Liu, F. Teng, C.H. Li, Y.H. Shen, Y.P. Yuan, *Adv. Mater. Interfaces* 2 (2015) 1500037–1500042.
- [61] Z.L. Wu, C.H. Wang, B. Zhao, J. Dong, F. Lu, W.H. Wang, W.C. Wang, G.J. Wu, J.Z. Cui, P. Cheng, *Angew. Chem. Int. Ed.* 55 (2016) 4938–4942.
- [62] G. Gai, G. Zhao, W. Zhou, Y. Liu, H. Pang, H. Zhang, D. Hao, X. Meng, P. Li, T. Kako, *Adv. Funct. Mater.* 26 (2016) 6822–6829.
- [63] Q.S. Ruan, W.J. Luo, J.J. Xie, Y.O. Wang, X. Liu, Z.M. Bai, C.J. Carmalt, J.W. Tang, *Angew. Chem. Int. Ed.* 56 (2017) 8221–8225.